Mechanosorptive Creep of Norway Spruce on the Tissue Scale Perpendicular to Grain

Alessia Ferrara[1] and Falk K. Wittel[2,*]

[1]ETH Zurich, Institute for Building Materials, HIF E 28, Laura-Hezner-Weg 7, 8093 Zurich, Switzerland ; ORCID: 0009-0003-9627-5200
[2]ETH Zurich, Institute for Building Materials, HIF E 28, Laura-Hezner-Weg 7, 8093 Zurich, Switzerland ; ORCID: 0000-0001-8672-5464
[*]Corresponding author: fwittel@ethz.ch

Abstract

Mechanosorptive creep strain (MCS) is a strain component that can dominate the overall deformation behavior of wood components under load and changing moisture. In this work, the MCS behavior of Norway spruce (*picea abies*) tissues is investigated for different anatomical directions perpendicular to grain and loading degrees (LD). The MCS is evaluated through a strain decomposition of the total strain, which is determined using a computer-controlled digital image correlation (DIC) system. We show that the common assumption of a scalar relation between mechanosorptive creep compliance (MCC) and the orthotropic, moisture-dependent elastic one (1) is refuted by experiments in different anatomical directions perpendicular to grain.

1 Introduction

The behavior of wood under both varying mechanical load and moisture content (mc or ω) is very rich. Unfortunately, this complexity is only weakly considered by constitutive models, primarily due to a sparse experimental basis with differing interpretations. However, it would be important, when thinking about the recent boost in timber engineering, where cross-laminated timber (CLT) and glue-laminated timber (GLT) products are used to build skyscrapers (2) or for self-shaping CLT that relies on moisture changes (3). The material symmetry of a growing tree results in an orthotropy with radial (R), tangential (T), and longitudinal (L) anatomic directions (4; 5). Typically, one distinguishes different deformation components like elastic, plastic, hygro-expansional, viscoelastic creep (VCS), and mechanosorptive creep strain (MCS) that add up to the total strain (1; 6; 7; 8). Note that combinations of VCS and MCS (9) or viscoplastic and plastic strain (10) were also proposed; however, these are ultimately different interpretations of the same experimental basis. In this work, we focus on the MCS that is often neglected in timber engineering, even though bending experiments have shown that the deflection due to MCS can be up to 20 times larger than that under constant climate (11). MCS is the creep strain that evolves due to moisture changes under load, which explains why an isolated determination is not possible. MCS is virtually time-independent and influenced by the magnitude of moisture change below fiber saturation and the moisture level, rather than by the moisture flux. Its origin within the hierarchical material is still not fully resolved, but observed on all scales, resulting in inter- and intra-scale interactions. The cellular tissue scale bridges tracheids and the macroscopic behavior, and thus deserves special attention that has not been given to MCS on the tissue scale in different anatomical directions in the past.

Mechanosorptive creep in wood was first described in the late 1950s and early 1960s by (12; 13). From the onset, researchers speculated on its relationship to the existence and change in hydrogen bond density associated with moisture changes. Reviews on MCS were published by (14; 15; 11; 16; 17). The latest review includes atomistic and micro-mechanical perspectives (18). In the past, several inconsistent theories have been proposed for the origin of MCS. (19) interpreted deformations in MCS tests on the molecular level with molecular kinetics theory and with a lenticular trellis model that can qualitatively explain observed processes. (20) proposed that the MCS is generated by slips between polymer chains that are cross-linked by hydrogen bonds. In this spirit, (16) proposed a slip-plane theory for localized slip planes forming in the S2 layer. However, MCS is already observed at stress levels below the threshold for slip-plane formation

and also under tension, where no slip-planes have been observed so far. In addition, it does not explain the difference between moisture-dependent VCS and MCS. (21) explained MCS on the cell wall ultra-structure, where, due to differential shrinkage of layers, relative slip between (ML+P+S1) and (S2+S3) layers could be triggered. Unfortunately, their validation is questionable due to possible preparation artefacts. (22) relates MCS to shear stress components along the cellulose-matrix interface and points to similarities between the mechanism generating the MCS and the ones responsible for the large plastic strains in wet compression wood loaded in tension, namely, breaking and reforming of hydrogen bonds between parallel polymer chains. (23) took up several of these ideas and proposed a fiber bundle model with moisture and history-dependent slip-stick behavior where elastic, swelling, plastic, VCS, and MCS emerge naturally from a single slip-stick mechanism.

Several interesting observations surround MCS, including larger creep rates for desorption than for absorption, the emergence of extremely large shear strains beyond typical failure limits, and the progressive reduction of MCS increments with increasing cycle number. (24) discovered an influence of the MCS on the VCS rate and reported on a limit for MCS (25; 26; 27; 28). However, the existence of an MCS limit has not been confirmed so far (29). At constant moisture, strains are frozen, but can be partially recovered after unloading through moisture cycles, with greater recovery during absorption. This phenomenon is also referred to as the moisture-induced shape memory effect, characterized by both recoverable and irrecoverable strains. In the FBM approach (23), this behavior emerges when slip-back events have lower thresholds than advancing slips.

Most MCS studies are made under bending to put the material in the L-direction simultaneously under tension and compression (30; 31; 32; 17; 33; 34). Inhomogeneous, evolving stress fields, strong moisture gradients due to transport, and deviating creep behavior under compression and tension complicate the interpretation of such experiments to an extreme extent, resulting in multiple misinterpretations of MCS in the past. However, some studies on purely tensile or compressive macroscopic samples, also in transverse directions, were made (35; 36; 37; 38; 39; 40), highlighting the importance of direct measurements in different anatomic directions. Unfortunately, many of these works are on different species, do not report on decomposed strains, or do not comprise a sufficient number of moisture cycles.

This study investigates the mechanosorptive creep behavior of Norway spruce on tissue samples to minimize the effect of moisture-gradient-induced creep due to residual stresses. It is focused on the two transverse anatomical directions (radial and tangential), where MCS is most pronounced, across various loading degrees (LD). A fully automated test rack with a computer-controlled digital image correlation (DIC) system and five parallel axes, located in a glove box with moisture control, ensures identical hygric and mechanical loading conditions across different realizations (41).

The mechanosorptive creep strain is extracted from the total strain via strain decomposition, employing a novel incremental scheme that not only mitigates the effects of inaccurate mapping of moisture content as a function of relative humidity $\omega(RH)$, since samples may not reach equilibrium under variable humidity, but also reduces uncertainty related to the elastic and hygroexpansion parameters. Then the mechanosorptive creep compliance (MCC) is modeled by a series of three Kelvin-Voigt (KV) type elements in response to moisture changes, rather than in the time domain (6). We show that the typical assumption of a scalar relation between MCC and the orthotropic, moisture-dependent elastic compliance tensor (1) is refuted by our experiments.

2 Materials and methods

Mechanosorptive creep in wood is among the most challenging phenomena to characterize experimentally. Its complexity arises from the intricate coupling between hygric and mechanical deformations, requiring highly controlled and sensitive measurement setups and advanced evaluation procedures for strain decomposition. First, we describe the preparation of samples for tensile creep testing (Sec. 2.1), along with the experimental setup. Since only relative humidity can be controlled in the climate chamber, the quantification highly depends on the accompanying results of the dynamic vapor sorption (DVS) measurements described in Sec. 2.2. This is fundamental, as moisture content is the control parameter for the evaluation procedure, namely the strain decomposition procedure for isolating the mechanosorptive strain from the total measured strain. Sec. 2.3 first describes the validation of the procedure on calculated clean data, and then its application to the real data of transverse strains.

2.1 Material selection and experimental setup

All samples were obtained from the same Norway spruce log used in our previous studies (42; 41). After conditioning from the green state to $65\,\%$RH/$20\,°\mathrm{C}$, small blocks ($(20 \times 15 \times 50)\,\mathrm{mm}^3$) were cut for slicing tissues in different anatomical orientations. The sample preparation followed the procedure described in (41) to obtain samples in transverse directions, namely *{RL,RT,TR}* (see Fig. 1), where the first letter defines the loading direction, and the second indicates the transverse width.

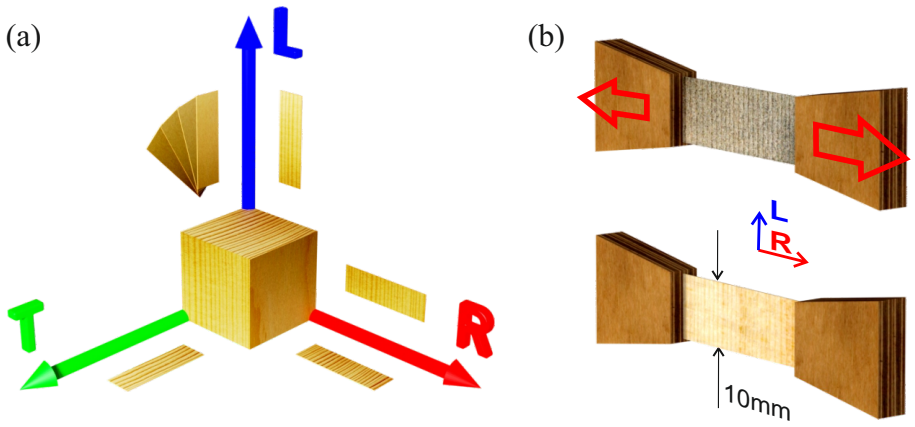

Figure 1: Spruce tissues for all combinations of directions *{LR,RL,RT,TR,LT,TL}* (a), and exemplary *RL* samples prepared with glued-on load application pieces from plywood, and speckled for DIC measurements via an airbrush (b).

The automated 5-axis creep-rack, mounted inside a climatized glove box (see Fig. 2a) was previously described in detail in (41) and also the sample geometry remains similar: $50\,\mathrm{mm}$ in length and $10\,\mathrm{mm}$ in width with thicknesses of about $0.35\,\mathrm{mm}$ to $0.40\,\mathrm{mm}$. A double-slice configuration, gluing the ends, was applied to all samples to increase the thickness. Samples were glued with a fixture to trapezoidal loading pieces of $2\,\mathrm{mm}$-thick plywood at their ends to ensure a smooth load introduction and sample alignment (see sample holder in Fig. 2b) and finally speckled with fine black and white acrylic paint to obtain the characteristic pattern for strain measurement via DIC.

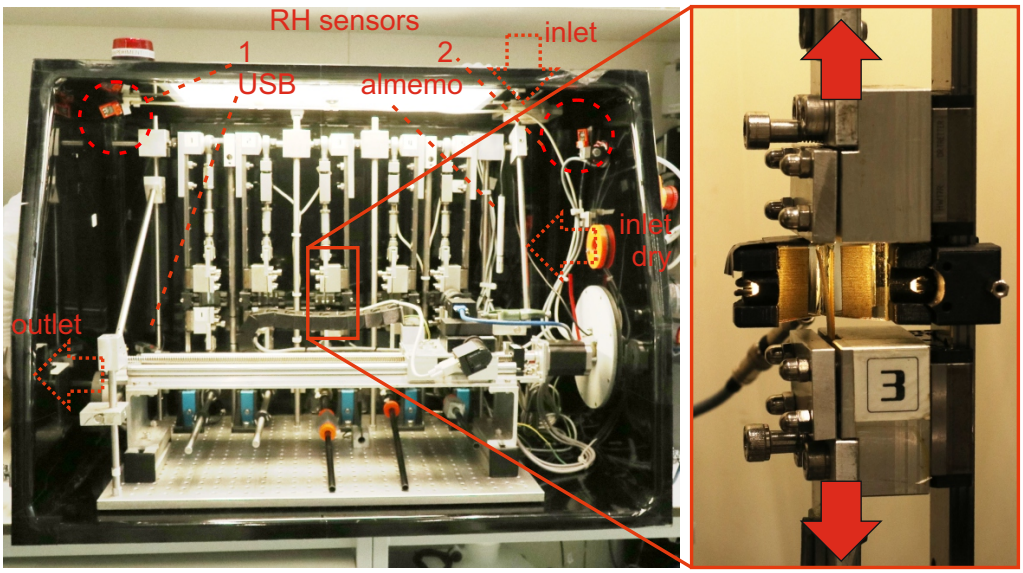

Figure 2: Custom-designed test rack for tensile creep testing on thin tissue samples, equipped with five sample holders (inset) to allow simultaneous testing of multiple samples. The humidity sensors (S1, S2), along with the inlet and outlet of the ventilation system, are marked in red to highlight their positions.

An overview of the samples that entered this study is provided in Tab. 1. Note that at least $n = 4$ for each case were valid, while experiments exhibiting early failure, evident pre-damage from sample preparation

or clamping, or unreliable DIC measurements were omitted.

Table 1: Sample sizes for the respective tissue types, grouped by loading degree (LD).

		LD [%]		
loading direction	**transverse direction**	**30**	**40**	**50**
R	*L*	5		4
R	*T*	4		5
T	*R*		4	

The samples were tested under changing humidity in a cyclic pattern between $30\,\%$ and $90\,\%$ RH at a period ΔT of about $2\,\mathrm{h}$ (see Sec. 2.2). Furthermore, two loading levels (LDs) corresponding to approximately 30 and $50\,\%$ of the tensile strength σ_{ii}^{f} measured at $90\,\%$ RH (42) were applied to *{RL,RT}*. For *TR*, however, only the $40\,\%$ LD yielded valid results. Higher loads caused the samples to fail right after the first moisture cycle, likely due to excessive stress concentrations near the clamps from hygroexpansion. Lower LDs, e.g. $30\,\%$, could not be tested reliably under these varying conditions as they approach the minimum load capacity of the testing rack. Once samples were loaded at $30\,\%$ RH, humidity was cycled between $30\,\%$ and $90\,\%$ RH, ramping up/down at $\pm 10\,\%$ RH steps every $4\,\mathrm{min}$ with $38\,\mathrm{min}$ hold periods at each extreme. This sequence was repeated 8-9 times under load, after which the load was released for 2 relaxation cycles.

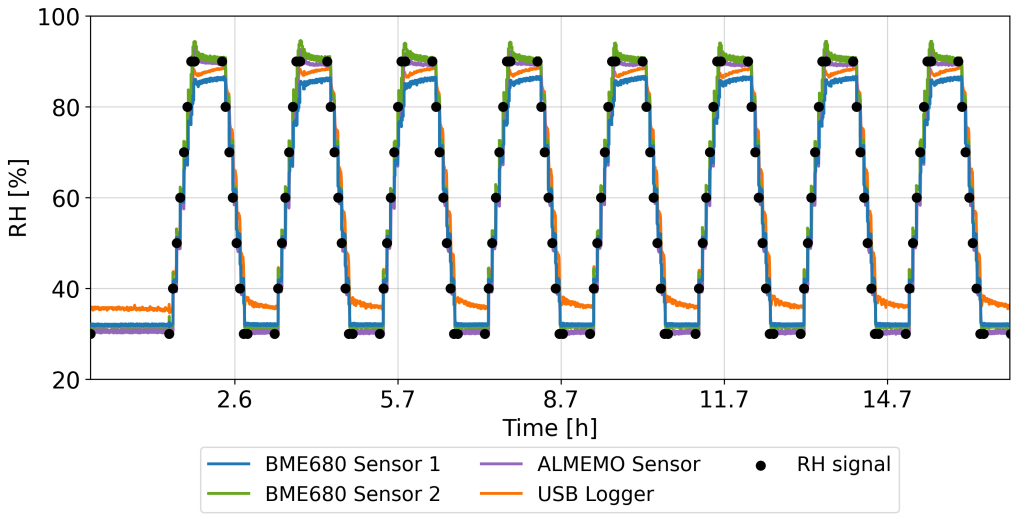

Figure 3: Time evolution of relative humidity (RH) inside the glove box measured by the two BME680 sensors (blue and green), the ALMEMO sensor (violet), and the USB data logger (orange). The black markers indicate the signals sent to the control system to set the target RH.

The relative humidity inside the glove box is controlled by a Python script on a Raspberry Pi 3B+ that obtains values from two moisture sensors (Bosch BME680, $\pm 3\%$ RH accuracy) located at opposite sides of the chamber, i.e. near the inlet and in the farthest corner from the in- and outlet (see Fig. 2a). Using their mean reading, the control system regulates humidity at a tolerance of $\pm 2\,\%$ by opening a valve to introduce dry air (at 10% RH) when RH exceeds the target or activating a moist air stream if RH falls below it. A ventilation system ensures uniform climatic conditions. The humidity control system was tested to verify its long-term stability and dynamic response for the mechanosorptive moisture-cycling protocol. The tests replicated the same moisture cycle of the mechanosorptive experiments, preceded by some hours at a constant RH. The measurements were verified using a moisture sensor (ALMEMO Ahlborn FH A646-E1) logged via the data logger ALMEMO 710, located near the top-right corner, and a USB sensor (USB data logger EL-USB-2) placed at the bottom of the glove box. Fig. 3 presents an example of RH data recorded for a $2\,\mathrm{h}$ hold at $30\,\%$ RH followed by 8 full cycles. The measurements from all sensors agree within a negligible discrepancy, demonstrating both the control system's rapid response to humidity changes and the ventilation system's ability to maintain rather uniform conditions in the box.

2.2 Sorptivity of spruce tissues

The evaluation of mechanosorptive tests requires the accurate mapping of moisture content ω with RH (or time), since under varying humidity conditions, the samples may not be fully equilibrated to each humidity step. For this purpose, tailored DVS measurements were conducted that followed the predefined RH profile of the test, using an automated sorption balance (DVS Advantage ET85, Surface Measurement Systems Ltd.). The results (staircase shaped datasets) are overlaid in Fig. 4a for direct comparison. After equilibrating at $30\,\%$ RH, moisture uptake closely follows the equilibrium curve in the initial sorption phase, indicating that the sample remains near equilibrium. However, as RH rises, the actual moisture content progressively deviates from the sorption curve, only reconverging by the end of the $90\,\%$ RH hold phase. During desorption, water removal proceeds more slowly due to the moisture-dependent diffusion coefficient (43). As a result, it fails to return to its equilibrium state by the end of the $30\,\%$ RH hold. In the subsequent sorption phase, moisture uptake follows a similar staircase pattern, reconverging to the same point by the end of the $90\,\%$ RH hold, repeating thereafter. Thus, the first sorption phase differs, while the desorption curves remain consistent. For comparison, the equilibrium sorption isotherm between $30\,\%$ and $90\,\%$ was measured, following the procedure outlined in (44) (grey dashed line in Fig. 4a).

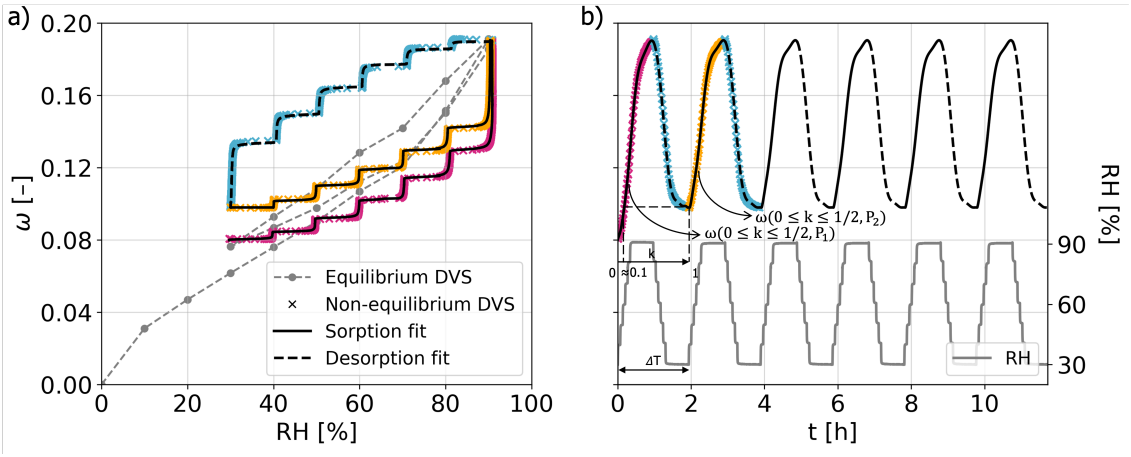

Figure 4: DVS test results on a *RL* tissue sample. (a) Moisture content ω as a function of relative humidity (RH): equilibrium DVS (grey dashed line) and non-equilibrium DVS (cross markers: magenta = first sorption $\omega(k, P_1)$, with $0 \leq k < 1/2$, orange = second sorption $\omega(k, P_2)$, light blue = desorption), with cubic spline fits for sorption (black solid line) and desorption (black dashed line). (b) Example of a periodic cubic-spline fit representing ω as a continuous function of time and RH history (grey solid line).

Since the actual evolution of mc during experimental humidity cycling diverges from the equilibrium isotherms, the non-equilibrium measurements are taken as reference for its mapping, but with the initial half-cycle being different from all subsequent ones. Moreover, because fitting ω as a function of time (periodic cubic spline) is more straightforward than fitting it against RH (staircase-shaped curve), the time-based spline is adopted for post-processing so all the strain components (see Sec. 2.3) are expressed as a function of time t and ω. Fig. 4b illustrates an example of this periodic time-based spline fit of ω. Since these measurements are representative for spruce, they were then applied to all sample types.

2.3 Incremental decomposition scheme for mechanosorptive strain calculation

The evaluation of the experimental data is based on two time series, one for each speckled surface with lens distortion correction applied. Surface strain fields are computed at each time t by DIC of the reference and current images using the Ncorr MATLAB package (45) (estimated strain accuracy of about $\pm 3 \cdot 10^{-5}$). A scalar strain value in the loading direction is calculated by averaging the strain field. The two surface scalars are further averaged to yield a single scalar tensile strain $\varepsilon^{tot}(t)$, as in our previous work (41). Finally, $\varepsilon^{tot}(t)$ is synchronized with moisture $\omega(t)$ and the corresponding stress σ, calculated from the initial cross section and the applied load.

The total strain ε^{tot} has to be decomposed into its hygroexpansion ε^{ω}, elastic ε^{el}, viscoelastic ε^{ve}, and

mechanosorptive ε^{ms} component, which are all strongly moisture-dependent, namely:

$$\varepsilon^{tot} = \varepsilon^{\omega} + \varepsilon^{el} + \varepsilon^{ve} + \varepsilon^{ms}. \tag{1}$$

Assuming that hygroexpansion, elasticity, and viscoelasticity are already well captured by existing constitutive models, mechanosorption remains the component to be identified. By rearranging Eq. 1, one can obtain $\varepsilon^{ms} = \varepsilon^{tot} - \varepsilon^{\omega} - \varepsilon^{el} - \varepsilon^{ve}$, but, in practice, ε^{ω}, ε^{el}, and ε^{ve} all depend on the moisture content. Therefore, any error in ω propagates into ε^{ms}. To reduce it, ω was accurately mapped using the experimental humidity profile (see Sec. 2.2), and a novel incremental decomposition procedure for calculating MCS is proposed and validated.

Building on the precise moisture mapping, the incremental scheme is founded on the observation that corresponding points in each humidity cycle occur under identical humidity conditions and, therefore, share the same moisture content, so they will have the same hygro-elastic strain. By summing the strain increases between corresponding points in consecutive humidity cycles, one can extract the VCS and MCS. To split off the VCS, its evolution must be calculated under varying moisture and load conditions. Note that plastic strain components are not considered separately and, if any, are comprised in the MCS.

To validate our procedure, we apply the measured moisture history $\omega(t)$ and a stress history $\sigma(t)$ to compute all strain components as functions of $\omega(t)$ (material parameters taken from *RL* samples) and superimpose them to obtain a total calculated strain ε^{*tot} (Eq. 1). In accordance with the analytical model of (6), the individual strain components are computed for any direction. They are summarized in scalar form, as only uniaxial situations are regarded:

ε^{ω} : The hygroexpansion strain is proportional to increments of moisture, as in

$$\varepsilon^{\omega}(\omega) = \alpha[\omega(t) - \omega_0], \tag{2}$$

where ω_0 is the initial reference moisture content and α is the hygro-expansion coefficient. α is assumed to remain constant and independent of variations in moisture. The values α_R=0.182; α_T=0.343 in $[\%/\%]$ are obtained from macroscale measurements of the same tree as in this study.

ε^{el} : The elastic strain is calculated from Hooke's law as

$$\varepsilon^{el}(\omega) = C_0^{-1}(\omega(t)) \cdot \sigma(t), \tag{3}$$

where the moisture-dependent elastic compliance $C_0^{-1}(\omega(t))$ is determined by a quadratic fit of the tensile elastic measurements (42), and then evaluated at $\omega(t)$.

ε^{ve} : The VCS is expressed by a series of $N = 4$ KV-elements, following previous studies (41; 46), in the time domain:

$$\varepsilon^{ve}(t) = \sum_{i=1}^{N} \varepsilon_i^{ve}(t) = \sigma \sum_{i=1}^{N} C_i^{-1}(1 - e^{-t/\tau_i}), \tag{4}$$

where ε_i^{ve}, C_i^{-1}, and τ_i are, respectively, the strain, compliance, and characteristic time of the i^{th}-element. While the characteristic times were fixed *a priori* to $\tau_i = [0.1, 1, 10, 100]$ in h, each moisture-dependent C_i^{-1} is obtained by a quadratic fit of the available data in (41), as for elastic compliances, and then evaluated at $\omega(t)$. Since both stress and compliance vary with time, each element is governed by the rate equation

$$\dot{\varepsilon}_i^{ve} + \frac{1}{\tau_i}\varepsilon_i^{ve} = \frac{1}{\tau_i} C_i^{-1}\sigma(t), \tag{5}$$

that gives for each finite time increment $\Delta t = t_{n+1} - t_n$

$$\varepsilon_{i,n+1}^{ve} = \varepsilon_{i,n}^{ve} + \frac{C_i^{-1}\sigma(t) - \varepsilon_{i,n}^{ve}}{\tau_i}\Delta t. \tag{6}$$

ε^{ms} : The MCS is formulated analogously to the VCS above, but in the moisture domain (1; 47; 6). It is modeled as a series of $M = 3$ KV-elements with fixed characteristic moistures $\mu_j = [1, 10, 100]$ in $[\%]$ (consistent with (6)) and compliance tensors C_j^{-1}:

$$\varepsilon^{ms}(\omega) = \sum_{j=1}^{M} \varepsilon_j^{ms}(\omega) = \sigma(t) \sum_{j=1}^{M} C_j^{-1}(1 - e^{\omega/\mu_j}), \tag{7}$$

where $C_j^{-1} = [1, 6, 8]$ in GPa^{-1} are arbitrarily chosen for the one-dimensional verification calculations. Note that for the experimental data, the C_j^{-1} are obtained by least-squares fits of the extracted ε^{ms}. Because both stress and compliance vary with moisture, each element is governed by the rate equation

$$\dot{\varepsilon}_j^{ms} + \frac{|\dot{\omega}|}{\mu_j}\varepsilon_j^{ms} = \frac{|\dot{\omega}|}{\mu_j} C_j^{-1}\sigma(t), \tag{8}$$

that gives for each finite moisture increment $|\Delta\omega| = |\omega_{n+1} - \omega_n|$ corresponding to $\Delta t = t_{n+1} - t_n$

$$\varepsilon_{j,n+1}^{ms} = \varepsilon_{j,n}^{ms} + \frac{|\Delta\omega|}{\Delta t}\frac{C_j^{-1}\sigma(t) - \varepsilon_{j,n}^{ms}}{\mu_j}\Delta t. \tag{9}$$

Each strain component is computed over $N_P = 20$ moisture cycles, 12 of which are conducted under load and 8 without load to allow for relaxation, as shown in Fig. 5. This data is now used for validating the strain decomposition procedure.

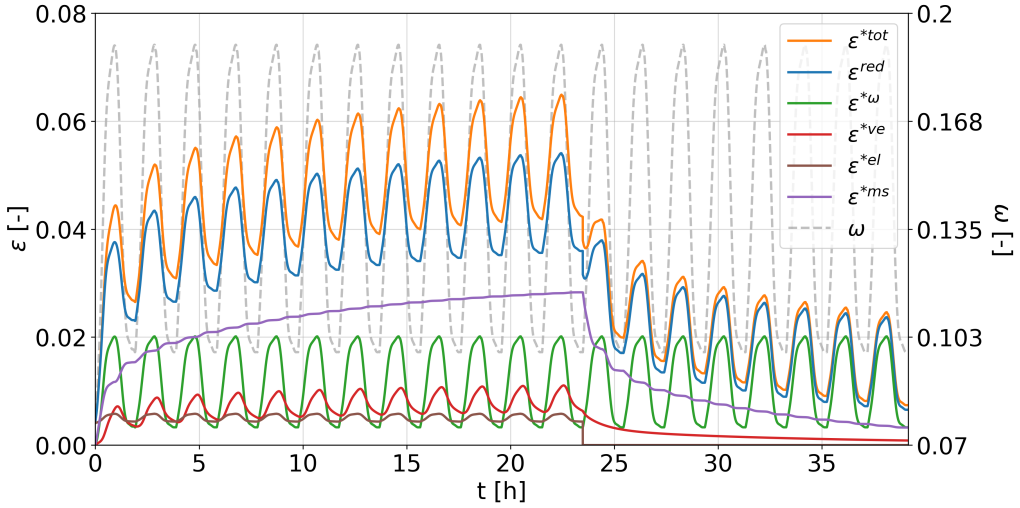

Figure 5: Example of evolution of calculated hygroexpansion ε^{ω}, elastic ε^{el}, viscoelastic ε^{ve}, mechanosorptive ε^{ms}, and the resulting total strain ε^{*tot} over $N_P = 20$ moisture cycles (12 under tensile load followed by 8 load-free) for validation purposes.

Starting from the total strain, either from the DIC measurements $\varepsilon^{tot}(t)$ or the calculated strain $\varepsilon^{*tot}(t)$ for validation purposes, the decomposition procedure outlined in Fig. 6 is applied to extract the MCS ε_{inc}^{ms}. As each cycle P_i, except the first half-cycle P_1 with $k \in [0, 1/2)$, undergoes an identical moisture evolution (see Fig. 4a) at the same relative cycle time k, the sample is at the same moisture state for each value of $k \in [0, 1]$ what corresponds the period ΔT. Therefore, respective strain differences at identical relative times k eliminate the hygro-elastic strain components $\varepsilon^{\omega+el}(k)$. What cannot be eliminated is the history-dependent VCS ε^{ve} that evolves during the hygro-mechanical loading. One has to calculate its evolution using Eqs. 4-6 with the moisture-dependent constitutive parameters obtained beforehand (41). Using the calculated VCS evolution, one can define a reduced strain $\varepsilon^{red}(t) = \varepsilon^{tot} - \varepsilon^{ve}$ for simplicity. $\varepsilon^{red}(t)$ is still composed of the hygro-elastic strain $\varepsilon^{\omega+el}$, which can be eliminated by the cyclic differences, the MCS, and possible plastic strains that remain a part of the MCS.

The MCS incremental decomposition procedure only works from cycle P_2 onwards, determining the cycle increments, while the MCS of cycle P_1 needs to be determined separately. The procedure is based on building templates Θ from the reduced strain $\varepsilon^{red}(t)$ that describe the repeating hygro-elastic strain $\varepsilon^{\omega+el}(k) = \varepsilon^{\omega}(k) + \varepsilon^{el}(k)$ per cycle. Hence, two templates are needed, one for cycle P_1 that is called Θ^I and one for all the other cycles called template Θ^{II}:

Θ^{II}: To obtain a smooth template for the hygro-elastic strain $\varepsilon^{\omega+el}(t)$, one can average over all cycles P_i with $i \geq 2$ at identical stress σ. However, the cycles are more alike at later stages, as the cyclic mechanosorptive strain increase decelerates, giving a cleaner $\varepsilon^{\omega+el}(k)$. Therefore, only the last few cycles under load enter the calculation. First one collapses the cycles by plotting them as a function of

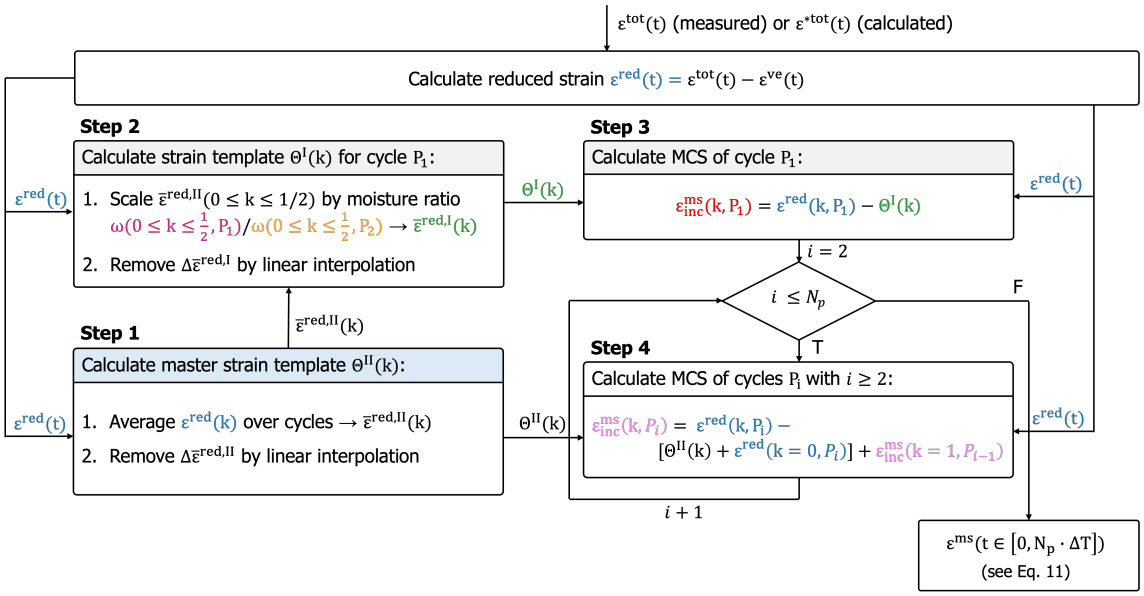

Figure 6: Workflow of the incremental scheme for mechanosorptive creep strain (MCS) calculation. Colors correspond to line segments and cycles in Figs. 4,7, and 8. Note that the calculated values, marked by a star, are not separately shown.

the relative cycle time k and shifting them so peak values of $\varepsilon^{red}(k)$ overlay. As they are quite similar and to reduce noise, an averaged $\overline{\varepsilon}^{red}(k)$ is calculated as shown in Fig. 7a (Step 1.1 in Fig. 6). This way, there is still a relative increase in MCS for the averaged $\overline{\varepsilon}^{red,II}(k)$ (since $\overline{\varepsilon}^{\omega+el}(k=0) = \overline{\varepsilon}^{\omega+el}(k=1)$) that corresponds to the averaged MCS increment $\Delta\overline{\varepsilon}^{red,II} = \overline{\varepsilon}^{red,II}(k=1) - \overline{\varepsilon}^{red,II}(k=0)$. To eleminate MCS from $\overline{\varepsilon}^{red,II}(k)$ a linear increase over the cycle up to $\Delta\overline{\varepsilon}^{red,II}$ is assumed and subtracted from $\overline{\varepsilon}^{red,II}(k)$, as shown in Fig. 7b (Step 1.2 in Fig. 6). The final template Θ^{II} is now only the mean hygroelastic strain $\overline{\varepsilon}^{\omega+el}(k)$ and can be applied for the decomposition of all cycles P_i with $i \geq 2$. Note that a new template is required for load changes, since the elastic strain ε^{el} differs.

Θ^I: Unfortunately, $\Theta^{II}(k)$ cannot be directly applied to cycle P_1, since $\omega(k)$ differs for cycle P_1 due to the initial sorption phase that starts at the equilibrium moisture content. We correct it by scaling the averaged strain $\overline{\varepsilon}^{red,II}(0 \geq k \geq 1/2)$, previously determined from the calculations of template Θ^{II} (Step 1.1) by the moisture ratio $\omega(0 \geq k \geq 1/2, P_1)/\omega(0 \geq k \geq 1/2, P_2)$ between the sorption phases of cycle P_1 and P_2, respectively, as shown in Fig. 7b (Step 2.1 in Fig. 6). Note that this superposition approach assumes linear correlations for $\varepsilon^{\omega}, \varepsilon^{el}$ with moisture ω within this $2\,\%$ moisture deviation. In the next step, the MCS increment of the first cycle $\Delta\overline{\varepsilon}^{red,I}$ needs to be subtracted, which only makes sense for identical moisture states. Therefore, one cannot take the value at $k=0$, but must take the one that corresponds to the first sorption phase, where the moisture is $\omega(k=1)$, as reference ($k \approx 0.1$). Once $\Delta\overline{\varepsilon}^{red,I}$ is determined, its linear increase over the entire cycle is subtracted from $\overline{\varepsilon}^{red,I}$, as shown in Fig. 7b (see Step 2.2 in Fig. 6) to obtain the strain template $\Theta^I(k)$ for cycle P_1. Note that possible non-linear behavior will result in small deviations during the cycle. However, values at every end of the cycle should be correct, except for a negligible discrepancy due to the linear nature of the correction procedure for the templates.

With the two templates Θ^I, Θ^{II}, one can now calculate the mechanosorptive strain for each cycle (Step 3 and 4 in Fig. 6) following

$$\varepsilon^{ms}_{inc}(k, P_i) = \begin{cases} \varepsilon^{red}(k, P_1) - \Theta^I(k) \text{if } i = 1 \\ \varepsilon^{red}(k, P_i) - [\Theta^{II}(k) + \varepsilon^{red}(k=1, P_{i-1})] + \varepsilon^{ms}(k=1, P_{i-1}) \text{if } i \geq 2 \end{cases} . \tag{10}$$

The overall MCS $\varepsilon^{ms}(t)$ is simply the consecutive sequence of all $\varepsilon^{ms}_{inc}(k, P_i)$ for cycles $i = 1 \dots N_P$ with the period ΔT that can be written with the indicator function $\mathbf{1}_{[a,b)}(t)$ that is defined as $\mathbf{1}_{[a,b)}(t) = 1$ if $a \leq t < b$, and $\mathbf{1}_{[a,b)}(t) = 0$ otherwise:

$$\varepsilon^{ms}_{inc}(t) = \sum_{i=1}^{N} \varepsilon^{ms}\left(\frac{t-(i-1)\Delta T}{\Delta T}, P_i\right) \cdot \mathbf{1}_{[(i-1)\Delta T,\, i\Delta T)}(t). \tag{11}$$

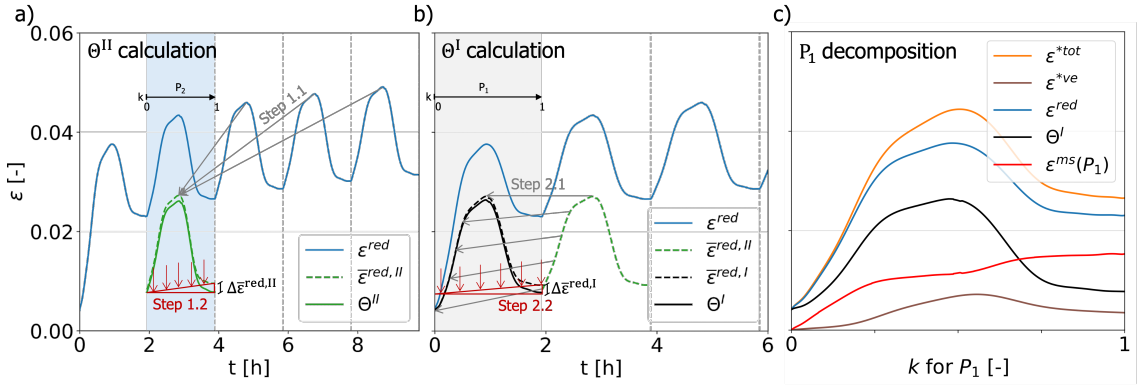

Figure 7: Incremental decomposition scheme for the calculation of mechanosorptive strain during moisture cycles P_i with Steps explained in Fig. 6. (a) Calculation of strain templates $\Theta^{II}(k)$ and (b) $\Theta^{I}(k)$. (c) Decomposition of cycle P_1 in relative cycle time k.

Note that for additional cycles at a different load, a new template, e.g. Θ^{III}, needs to be determined and those cycles need to be appended. This was made for the recovery part with no load, but not explicitly shown for compactness, as the procedure is identical.

Now that the decomposition procedure is complete, it is applied to the calculated total strain for validation purposes. The resulting MCS $\varepsilon^{ms}(t)$ from the strain decomposition is confronted in Fig. 8 with the calculated MCS $\varepsilon^{*ms}(t)$, which was part of $\varepsilon^{*tot}(t)$. The curves align remarkably well, confirming the validity of the incremental decomposition scheme. This approach also remains valid during unloading and, more generally, for any change in load throughout the experiment, provided that a new template is generated. When determining the parameters of the mechanosorptive KV-model (see Eq. 7) one obtains from the fitting the optimized parameters $C_j^{-1} = [0.8, 6.1, 7.9]\,\mathrm{GPa}^{-1}$, which are in close agreement with those used to calculate $\varepsilon^{ms}(t)$ ($C_j^{-1} = [1, 6, 8]\,\mathrm{GPa}^{-1}$).

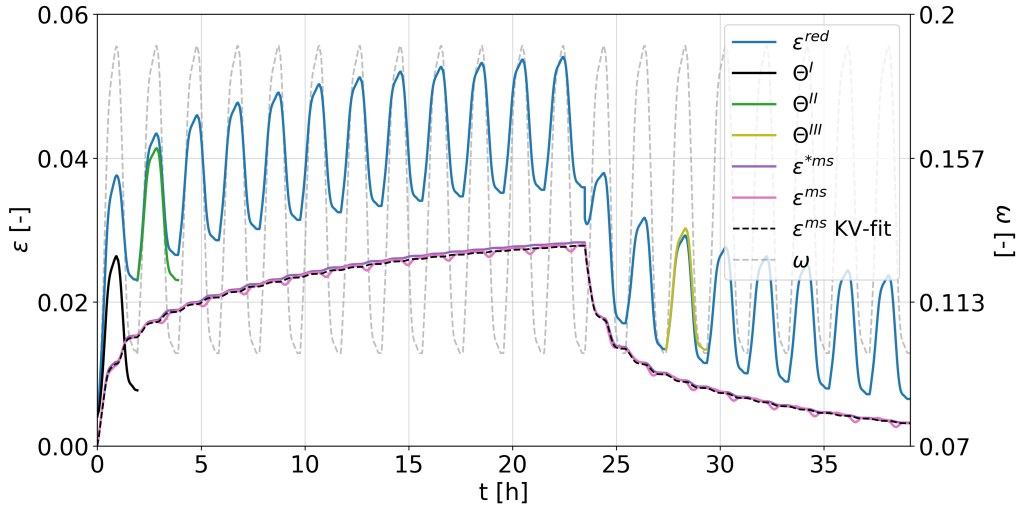

Figure 8: Comparison of calculated mechanosorptive strain $\varepsilon^{*ms}(t)$ with the extracted one $\varepsilon^{ms}(t)$ and its Kelvin–Voigt model fit for moisture cycles under load and recovery, as well as strain templates Θ^{I}-Θ^{III}.

The validated decomposition procedure can now be applied to noisy experimental $\varepsilon^{tot}(t)$ data from DIC, synchronized with the corresponding $\sigma(t)$ and $\omega(t)$ recordings. Finally, $\varepsilon^{ms}(t)$ is modeled using Eq. 7, consistently employing the characteristic moistures $\mu_j = [1, 10, 100]$ %, while the unknown parameters C_j^{-1} are determined via least-squares fitting analogous to the verification example. Finally, average MCS are computed across all samples for each investigated situation from the individual KV-series, and a mean KV-series $\bar{\varepsilon}^{ms}(t)$ is obtained by fitting the average curve. The MCS are converted into compliance $M_c(t)$ by dividing the strain by the applied stress and compared with the elastic compliances.

3 Results and Discussion

With this experimental setup, we can investigate how moisture changes under mechanical load influence the creep behavior of different spruce tissues in the transverse directions *{RL, RT, TR}*, where the MCS is most pronounced, and explore the dependence on the loading degree LD. Fig. 9 provides an overview of all results. First, the isolated mechanosorptive strains $\varepsilon^{ms}(t)$ through successive moisture cycles are shown for all samples of each investigated situation (Fig. 9a). These curves were obtained by applying the incremental decomposition procedure from Sec. 2.3 to the total strains $\varepsilon^{tot}(t)$ measured by DIC for each sample. Note that one *RT* sample under 30% LD and all unloading phases yielded unreliable data and were therefore excluded from the final evaluation. Although the incremental procedure is valid for any load change, two unloading cycles proved insufficient to resolve MCS increments during unloading with an acceptable accuracy.

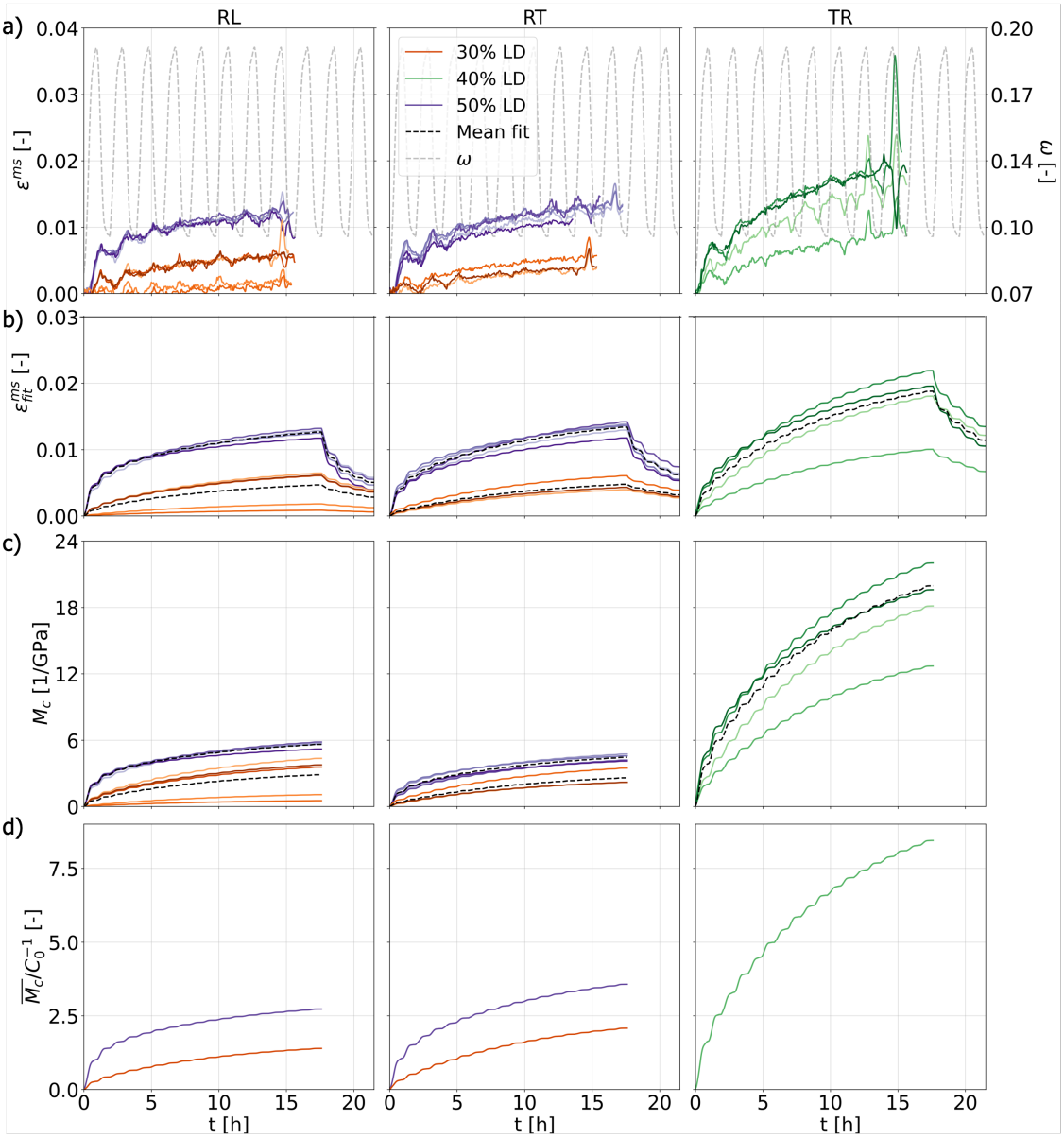

Figure 9: Evolution of mechanosorptive strain and compliance under cyclic humidity and different loading degrees LD (30 and $50\,\%$ for *{RL,RT}*, $40\,\%$ for *TR*). (a) Mechanosorptive strains ε^{ms} from incremental calculation scheme. (b) Fitted strains ε^{ms}_{fit} from Kelvin-Voigt model. (c) Mechanosorptive compliances M_c in GPa^{-1}. (d) Normalized compliances $\overline{M_c}/C_0^{-1}$ using C_0^{-1} from (42) at 0.08 moisture content.

The MCS were fitted to the three-element KV-model described in Sec. 2.3. Fig. 9b shows the strains computed via Eq. 7 using the fitted compliances C_j^{-1}, alongside the mean fitted response for each combination

of tissue type and LD. Note that one can calculate the average MCS response for the moisture history of this study at arbitrary times using the KV-element compliances from Table 2 and Eq. 7. This fitting procedure filters noise in the raw data and gives the possibility to extend the dataset to the relaxation phase, where load is removed and MCS decreases. It is evident that in the R-direction, higher applied loads result in increased creep deformation. At first glance, the MCS of *RL* and *RT* appear similar for each LD, but *RL* samples are actually subjected to lower absolute load due to their lower strength compared to *RT* (42). When considering the tangential orientation, *TR* exhibits higher strain at $40\,\%$ LD than the radial tissues at $50\,\%$ LD.

Table 2: Element compliances C_j^{-1} in GPa^{-1} of Kelvin-Voigt series fits of the average creep response for varying loading degrees LD (30 and $50\,\%$ for *{RL,RT}*, $40\,\%$ for *TR*) under moisture cycling between $30\,\%$ and $90\,\%$ RH. For each case, the mean coefficient of determination R^2 represents the average of the R^2 values from the fits to the individual experiments.

loading direction	transverse direction	LD [%]	$\mathbf{C_j^{-1}}$ [$\mathbf{GPa^{-1}}$]	Mean $\mathbf{R^2}$
R	*L*	30%	[1.3·1×10^{-3}, 3.7·1×10^{-1}, 3.1]	0.7
R	*L*	50%	[2.6·1×10^{-3}, 2.4, 3.9]	0.9
R	*T*	30%	[2.2·1×10^{-2}, 2.4·1×10^{-3}, 2.5]	0.6
R	*T*	50%	[1.2·1×10^{-4}, 1.6, 3.8]	0.9
T	*R*	40%	[1.4·1×10^{-1}, 2.2, 20.2]	0.9

The difference between anatomical directions is even more expressed for the mechanosorptive compliance (MCC) curves $M_c(t)$ (see Fig. 9c), which were calculated from the ratio of the fitted strains and the applied stress during the loading phase. M_c in the R-direction remains multiple times lower than the one in the tangential direction, mirroring trends reported for both elastic and viscoelastic deformations (42; 41) as creep under constant or changing moisture involves micro-structural adjustments of the cellular structure similar to elastic deformation. In the transverse direction, deformation is mainly governed by cell wall bending inducing stress localization, while radial loading also induces stretching through undulating load paths, enhancing performance and making the R-direction stiffer than T (48). Moreover, microstructural features such as rays strongly affect compliance in thin spruce samples: under radial loading they stretch and contract, under tangential loading they open acting like microstructural voids. Interestingly, *RL* exhibits greater compliance than *RT*, despite sharing the same loading axis, because slicing exposes cut-open cells and rays across the surface of *RL*, unlike in *RT* where they appear only at the nattow edges (41). The MCC curves for different load levels become closer but do not fully collapse, as in the case of viscoelastic creep compliances (41), indicating that the mechanosorptive response does not follow a simple linear scaling regime.

Finally, to show how MCC scales with the elastic compliances C_0^{-1} reported in our previous work (42), Fig. 9d gives the ratio $\overline{M_c}(t)/C_0^{-1}$, where $\overline{M_c}(t)$ is the average of the fitted MCC and a constant value of $C_0^{-1}(\omega = 0.08)$. The rise of the normalized MCC underscores that moisture history affects mechanosorptive but not elastic compliance. Moreover, the relevance of the moisture history depends on the orientation, with the T-direction exhibiting a surprisingly large amplification up to a factor of 9 in our loading sequence. Clearly, additional moisture cycles under load would result in even higher values. In our data, we cannot therefore observe any limit for MCS as reported by (25; 26; 27). This could be due to a high LD or the uniaxial stress case that we could realize. Note that normalization by compliance values at other moisture states or even following the moisture evolution only changes the picture in a negligible way.

Although the MCS continuously increases over successive moisture cycles, its rate exhibits a distinct behavior, characterized by a sharp rise during the first sorption, followed by a continued but gradually decreasing peak rate. Fig. 10 illustrates the evolution of the mean fitted MCS rate $\Delta\bar{\varepsilon}_{fit}^{ms}/\Delta t$. In each direction, the initial steep rise is evident up to a peak, after which the rate decelerates as the mc approaches its maximum. This again highlights the dependence of MCS on moisture change. When mc reverses and decreases, the rate rises sharply again before slowing near the minimum mc at the end of the lower holding phase. The markedly high MSC rate peak highlights the stronger impact of the initial phase of the first moisture cycle. By contrast, subsequent cycles show much smaller and progressively diminishing peaks, with no significant difference between sorption and desorption. Interestingly, the T-direction exhibits a less pronounced decrease in rate and maintains a higher rate in the later cycles compared to the R-direction, despite being at a different LD. Moreover, a clear LD-related pattern emerges: the lower the LD, the lower the rate but also the less steep the decline of the peaks. Note that the MCS increment corresponds to the area underneath

the rate curves.

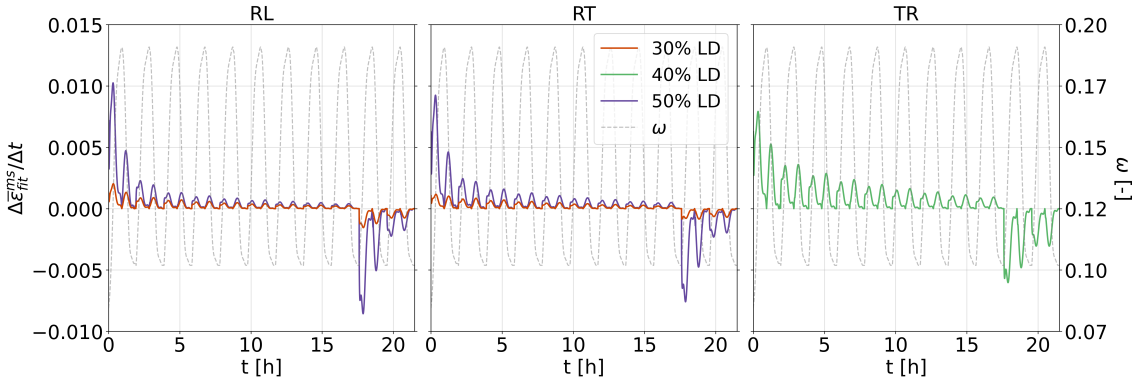

Figure 10: Evolution of mean fitted mechanosorptive strain rate $\Delta\bar{\varepsilon}^{ms}_{fit}/\Delta t$ under cyclic humidity and different loading degrees LD (30 and $50\,\%$ for *{RL,RT}*, $40\,\%$ for *TR*).

To relate MCS to the other strain components, one can plot the absolute values of strain for the different directions and their decomposition into the different strain contributions. In Fig. 11, the calculated total strain ε^{*tot} is obtained as the sum of the mean fitted MCS ε^{ms}_{fit} (at $50\,\%$ LD for *RL*, *RT* and $40\,\%$ LD for *TR*) and the other calculated strain components ($\varepsilon^{*\omega}$, ε^{*el}, and ε^{*ve}) according to Eqs. 2–4. It is striking to observe that MCS slightly exceeds the VCS and the elastic one by far. This points to the importance of considering MCS in the transverse directions in a dedicated way in constitutive models of wood for timber engineering.

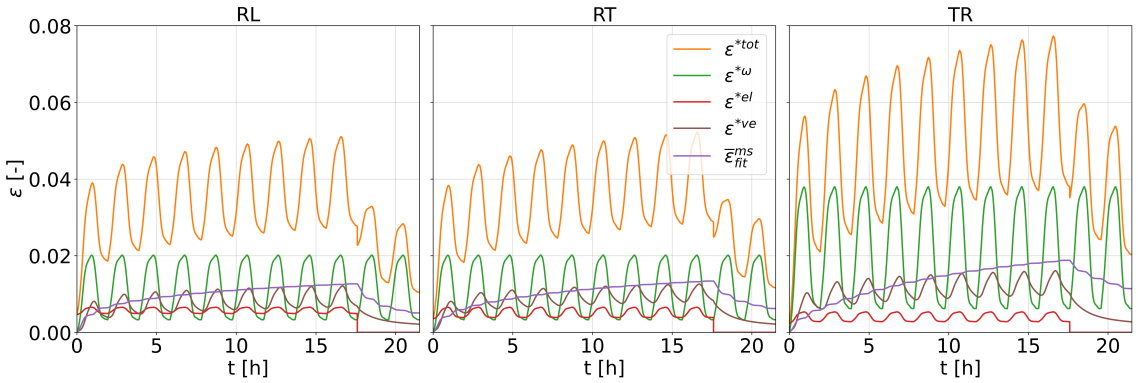

Figure 11: Calculated total strain ε^{*tot} as the sum of calculated hygroexpansion $\varepsilon^{*\omega}$, elastic ε^{*el}, and viscoelastic ε^{*ve} strains, and the mean fitted mechanosorptive strain $\bar{\varepsilon}^{ms}_{fit}$, for *RL*, *RT* at $50\,\%$ loading degree and *TR* at $40\,\%$.

4 Conclusion

This study sheds light on the complex phenomena of creep under changing climatic conditions in spruce. It was possible to obtain continuous strain data for a large number of samples and relatively long testing periods due to the full automation of a climatized test rack. Additionally, multiple loading axes assure identical moisture histories of the samples. The isolation of MCS in wood is non-trivial, as the measured total strain is composed of hygroexpansion, elastic, viscoelastic, and mechanosorptive strain components. The decomposition requires a good knowledge of the viscoelastic behavior of the samples, as it can only be separated by calculating its evolution, as well as the evolution of moisture. By analytically generating clean data from a rheological model (6), we developed and validated a novel incremental strain decomposition scheme that reduces the effects of non-equilibrium moisture mapping under variable RH and reduces uncertainty in the hygro-elastic behavior. Accompanying DVS tests using the identical cycling RH profile ensured precise moisture mapping. Nevertheless, the role of plastic strain increments remains uncertain.

Our experiments reveal striking directional dependencies in mechanosorptive creep, most notably a dominant compliance in the T-direction that cannot be explained by elastic analogies alone or compliance changes under respective moisture states. In principle, MCC increases only with humidity changes and is time-independent, but since the samples are never fully equilibrated (see Fig. 4), one cannot expect plateaus. This points to possible size effects that require further investigation. Our data shows that MCS rates under sorption surpass the ones under desorption only for the first cycle in loading and relaxation. Consecutive cycles do exhibit identical rates without any dominance. Moreover, at the cell-wall level, internal stresses may alter sorptive behavior (49), with volumetric stress locally shifting moisture content: higher in tension and lower in compression. This disrupts the assumption of constant moisture fields within the cell wall and causes tracheid corners acting as hinges to soften and amplify directional effects. These effects are further superimposed with residual stresses from delayed moisture equilibration, which can drive creep strains. This clearly disproves the common assumption of a simple scalar relationship between elastic and mechanosorptive compliance tensors and highlights a lack of understanding of creep deformation mechanisms on the cellular scale.

While this work only explored the transverse directions, future work should be extended to the longitudinal direction, as strain variations in the L-direction were beyond the accuracy of our experimental setup. Isolated tissues, namely early, transition, and late wood tissues perpendicular to grain, would also be very interesting; however, the load ranges were below the experimental design. Such investigations could clarify the contribution of each isolated tissue to the cumulative behavior of a growth ring and further advance the understanding of mechanosorptive creep behavior across all anatomical directions and tissue types. With results from accompanying plasticity experiments on the tissue scale, one could further decompose the total strain by subtracting the calculated plastic evolutions from MCS. Finally, an advanced cellular model that incorporates stress-sorption couplings could shed light on the directional dependencies.

Data availability

The datasets can be obtained from
DOI: 10.17632/rsrsw8h7mv.1, and the analysis tool from DOI: doi.org/10.5281/zenodo.17160378.

Acknowledgments

The authors acknowledge the Swiss National Science Foundation for funding this work under SNF grant 200021192186 "Creep behavior of wood on multiple scales". They also acknowledge Prof. Dr. Ingo Burgert for his valuable advice and Christopher Dreimol for conducting the dynamic vapor sorption tests.

References

[1] Stefania Fortino, Florian Mirianon, and Tomi Toratti. A 3D moisture-stress FEM analysis for time dependent problems in timber structures. *Mechanics of Time-Dependent Materials*, 13(4):333–356, 2009.

[2] SebastiÃ¡n Villamizar SantamarÃa. High-rise buildings made out of wood. *Nature Cities*, 1(5):332–333, 2024.

[3] Philippe GrÃ¶nquist, Dylan Wood, Mohammad M. Hassani, Falk K. Wittel, Achim Menges, and Markus RÃ¼ggeberg. Analysis of hygroscopic self-shaping wood at large scale for curved mass timber structures. *Science Advances*, 5(9):eaax1311, 2019.

[4] Peter Niemz, Alfred Teischinger, and Dick Sandberg, editors. *Springer Handbook of Wood Science and Technology*. Springer Handbooks. Springer International Publishing, 2023.

[5] Peter Niemz, Alfred Teischinger, and Dick Sandberg, editors. *Wood Material and Processing Data: The Most Relevant Data, Tables, and Figures*. Springer Nature Switzerland, 2025.

[6] Mohammad Masoud Hassani, Falk K. Wittel, Stefan Hering, and Hans J. Herrmann. Rheological model for wood. *Computer Methods in Applied Mechanics and Engineering*, 283:1032–1060, 2015.

[7] Peter Mackenzie-Helnwein and Antti HanhijÃ¤rvi. Computational analysis of quality reduction during drying of lumber due to irrecoverable deformation. II: Algorithmic aspects and practical application. *Journal of Engineering Mechanics*, 129(9):1006–1016, 2003.

[8] Susanne Reichel and Michael Kaliske. Hygro-mechanically coupled modelling of creep in wooden structures, Part I: Mechanics. *International Journal of Solids and Structures*, 77:28–44, 2015.

[9] Vanessa Angst and Kjell Arne Malo. Moisture-induced stresses in glulam cross sections during wetting exposures. *Wood Science and Technology*, 47(2):227–241, 2013.

[10] Susanne Reichel and Michael Kaliske. Hygro-mechanically coupled modelling of creep in wooden structures, Part II: Influence of moisture content. *International Journal of Solids and Structures*, 77:45–64, 2015.

[11] P. U. A. Grossman. Requirements for a model that exhibits mechano-sorptive behaviour. *Wood Science and Technology*, 10(3):163–168, 1976.

[12] L. D. Armstrong and R. S. T. Kingston. Effect of Moisture Changes on Creep in Wood. *Nature*, 185(4716):862–863, 1960.

[13] L. D. Armstrong and G. N. Christensen. Influence of Moisture Changes on Deformation of Wood Under Stress. *Nature*, 191(4791):869–870, 1961.

[14] A.P. Schniewind. Recent progress in the study of the rheology of wood. *Wood Science and Technology*, 2:188–206, 1968.

[15] Siegfried M. Holzer, Joseph R. Loferski, and David A. Dillard. A review of creep in wood: Concepts relevant to develop long-term behavior predictions for wood structures. *Wood and Fiber Science*, 21(4):376–392, 2007.

[16] P. Hoffmeyer and R. W. Davidson. Mechano-sorptive creep mechanism of wood in compression and bending. *Wood Science and Technology*, 23(3):215–227, 1989.

[17] A. MÃ¥rtensson. Mechano-sorptive effects in wooden material. *Wood Science and Technology*, 28:437â€“449, 1994.

[18] Parviz Navi and Stefanie Stanzl-Tschegg. Micromechanics of creep and relaxation of wood. A review COST Action E35 2004â€“2008: Wood machining â€“ micromechanics and fracture. *Holzforschung*, 63(2):186–195, 2009.

[19] J. D. Boyd. An anatomical explanation for visco-elastic and mechano-sorptive creep in wood, and effects of loading rate on strength. In P. Baas, editor, *New Perspectives in Wood Anatomy: Published on the occasion of the 50th Anniversary of the International Association of Wood Anatomists*, Forestry Sciences, pages 171–222. Springer Netherlands, Dordrecht, 1982.

[20] P. Navi, V. Pittet, and C.J.G. Plummer. Transient moisture effects on wood creep. *Wood Science and Technology*, 36(6):447–462, 2002.

[21] J. Mukudai and S. Yata. Modeling and simulation of viscoelastic behavior (tensile strain) of wood under moisture change. *Wood Science and Technology*, 20(4):335–348, 1986.

[22] Kenneth M. Entwistle. The mechanosorptive effect in pinus radiata D. Don. *Holzforschung*, 59(5):552–558, 2005.

[23] Júlio O. Amando de Barros and Falk K. Wittel. Unifying model for the rheological behavior of hygroresponsive materials. *Physical Review E*, 109:044139, 2024.

[24] A. Hanhijirvi and D Hunt. Experimental indication of interaction between viscoelastic and mechano-sorptive creep. *Wood Science and Technology*, 32:57–70, 1998.

[25] D. G. Hunt. Limited mechano-sorptive creep of beech wood. *Journal of the Institute of Wood Science*, pages 136–138, 1980.

[26] D. G. Hunt. Linearity and non-linearity in mechano-sorptive creep of softwood in compression and bending. *Wood Science and Technology*, 23(4):323–333, 1989.

[27] D. G. Hunt. A unified approach to creep of wood. *Proceedings of the Royal Society of London. Series A: Mathematical, Physical and Engineering Sciences*, 455(1991):4077–4095, 1999.

[28] D. G. Hunt and C. F. Shelton. Longitudinal moisture-shrinkage coefficients of softwood at the mechano-sorptive creep limit. *Wood Science and Technology*, 22(3):199–210, 1988.

[29] S. Mohager and T. Toratti. Long term bending creep of wood in cyclic relative humidity. *Wood Science and Technology*, 27(1):49–59, 1992.

[30] C. Bengtsson. Mechano-sorptive bending creep of timber â€“ influence of material parameters. *Holz als Roh- und Werkstoff*, 59(4):229–236, 2001.

[31] P. Koc and M. HouÅ¡ka. Characterization of the sorptive properties of spruce wood by the inverse identification method. *Holz als Roh- und Werkstoff*, 60(4):265–270, 2002.

[32] Mladen HouÅ¡ka. Mechano-sorptive effect in wood. *Journal of Mechanical Engineering*, 43(5):193–202, 1997.

[33] Romain RÃ©mond, Mariella De La Cruz, Daniel AlÃ©on, and Patrick PerrÃ©. Investigation of oscillating climates for wood drying using the flying wood test and loaded beams: need for a new mechano-sorptive model. *Maderas. Ciencia y tecnologÃa*, 15:269–280, 2013.

[34] Yaguang Zhou, Masami Fushitani, Takafumi Kubo, and Masayuki Ozawa. Bending creep behavior of wood under cyclic moisture changes. *Journal of Wood Science*, 45(2):113–119, 1999.

[35] Sabina Huc and Staffan Svensson. Coupled two-dimensional modeling of viscoelastic creep of wood. *Wood Science and Technology*, 52(1):29–43, 2018.

[36] Natalia PÃ©rez-Pena, Franz Segovia, Carlos Salinas, and RubÃ©n AnanÃas. Perpendicular mechano-sorptive strains during moisture desorption from eucalyptus nitens specimens. *BioResources*, 11(4):8277–8284, 2016.

[37] A. Ranta-Maunus. Rheological behaviour of wood in directions perpendicular to the grain. *Materials and Structures*, 26(6):362–369, 1993.

[38] S. Svensson and T. Toratti. Mechanical response of wood perpendicular to grain when subjected to changes of humidity. *Wood Science and Technology*, 36(2):145–156, 2002.

[39] T. Toratti and S. Svensson. Mechano-sorptive experiments perpendicular to grain under tensile and compressive loads. *Wood Science and Technology*, 34(4):317–326, 2000.

[40] Qinglin Wu and Michael R. Milota. Mechano-sorptive deformation of douglas-fir specimens under tangential tensile stress during moisture adsorption. *Wood and Fiber Science*, 28(1):128–132, 2007.

[41] Alessia Ferrara and Falk K. Wittel. Tensile creep of norway spruce on the tissue scale. *Mechanics of Time-Dependent Materials*, 29(2):36, 2025a.

[42] Alessia Ferrara and Falk K. Wittel. Micro-mechanical tests on tissue slices of Norway spruce: tensile and shear performance. *Holzforschung*, 78(11-12):624–630, 2024.

[43] Christen Skaar. *Wood-Water Relations*. Springer Series in Wood Science. Springer-Verlag, Berlin Heidelberg, 1988.

[44] Sophie Marie Koch, Christopher Hubert Dreimol, Christian Goldhahn, Aline Maillard, Andrina Stadler, Tina Künniger, Philippe Grönquist, Maximilian Ritter, Tobias Keplinger, and Ingo Burgert. Biodegradable and flexible wood-gelatin composites for soft actuating systems. *ACS Sustainable Chemistry & Engineering*, 12(23):8662–8670, 2024.

[45] J. Blaber, B. Adair, and A. Antoniou. Ncorr: Open-Source 2D Digital Image Correlation Matlab Software. *Experimental Mechanics*, 55(6):1105–1122, 2015.

[46] Alessia Ferrara and Falk K. Wittel. Orthotropic viscoelastic creep in cellular scaffolds. *Acta Mechanica*, 2025b. Under review, as preprint https://doi.org/10.48550/arXiv.2507.01071.

[47] Antti HanhijÃ¤rvi and Peter Mackenzie-Helnwein. Computational analysis of quality reduction during drying of lumber due to irrecoverable deformation. I: Orthotropic viscoelastic-mechanosorptive-plastic material model for the transverse plane of wood. *Journal of Engineering Mechanics*, 129(9):996–1005, 2003.

[48] Lorna J. Gibson and Michael F. Ashby. *Cellular Solids: Structure and Properties*. Cambridge University Press, Cambridge, 2nd ed. edition, 1997.

[49] Wilfred W. Barkas. *The swelling of wood under stress*. H.M. Stationery Office, Great Britain. Forest Products Research Board, 1949.